

Dynamic Feature-based Deep Reinforcement Learning for Flow Control of Circular Cylinder with Sparse Surface Pressure Sensing

Qiulei Wang¹, Lei Yan¹†, Gang Hu^{1,2,3}‡, Wenli Chen^{3,4}, Jean Rabault⁵, and Bernd R. Noack⁶

¹School of Civil and Environmental Engineering, Harbin Institute of Technology, Shenzhen 518055, China

²Guangdong Provincial Key Laboratory of Intelligent and Resilient Structures for Civil Engineering, Harbin Institute of Technology, Shenzhen, 518055, China

³Guangdong-Hong Kong-Macao Joint Laboratory for Data-Driven Fluid Mechanics and Engineering Applications, Harbin Institute of Technology, Shenzhen 518055, China

⁴Key Laboratory of Smart Prevention and Mitigation of Civil Engineering Disasters, the Ministry of Industry and Information Technology, Harbin Institute of Technology, Harbin, 150090, China

⁵Information Technology Department, Norwegian Meteorological Institute, Oslo, Norway

⁶School of Mechanical Engineering and Automation, Harbin Institute of Technology, Shenzhen 518055, China

Abstract

This study proposes a self-learning algorithm for closed-loop cylinder wake control targeting lower drag and lower lift fluctuations with the additional challenge of sparse sensor information, taking deep reinforcement learning as the starting point. DRL performance is significantly improved by lifting the sensor signals to dynamic features (DF), which predict future flow states. The resulting dynamic feature-based DRL (DF-DRL) automatically learns a feedback control in the plant without a dynamic model. Results show that the drag coefficient of the DF-DRL model is 25% less than the vanilla model based on direct sensor feedback. More importantly, using only one surface pressure sensor, DF-DRL can reduce the drag coefficient to a state-of-the-art performance of about 8% at $Re = 100$ and significantly mitigate lift coefficient fluctuations. Hence, DF-DRL allows the deployment of sparse sensing of the flow without degrading the control performance. This method also shows good robustness in controlling flow under higher Reynolds numbers, which reduces the drag coefficient by 32.2% and 46.55% at $Re = 500$ and 1000, respectively, indicating the broad applicability of the method. Since surface pressure information is more straightforward to measure in realistic scenarios than flow velocity information, this study provides a valuable reference for experimentally designing the active flow control of a circular cylinder based on wall pressure signals, which is an essential step toward further developing intelligent control in realistic multi-input multi-output (MIMO) system.

† Email address for correspondence: 180410212@stu.hit.edu.cn

‡ Email address for correspondence: hugang@hit.edu.cn

1. Introduction

Flow control has been a popular research area of great academic and industrial interest, which can be divided into passive flow control and active flow control on the basis of whether external energy input is necessary. Passive control has the advantages of requiring no energy, being easy to set up, and having low cost, but if the actual situation of the flow field differs from that expected, the control is often difficult to achieve the best effect. Active control can be divided into open-loop control and closed-loop control according to whether it is necessary to obtain feedback information from the flow field and adjust the flux of the actuator (Duriez *et al.* 2017). It has been found that compared with open-loop control, closed-loop active control has a robust adaptive ability, which can give full play to the potential of the actuator with a small amount of energy input. For example, Korkischko & Meneghini (2012) has presented a sequence of experiments on the flow around a cylinder, which included MSBC (Moving Surfaces Boundary Control). This method involved injecting momentum into the boundary layer of the cylinder by using two rotating cylinder modules, thereby delaying separation and preventing vortices. Nevertheless, the complexity of the nonlinear Navier-Stokes equations leads to a flow field with high dimension and multimodal characteristics, thus making it challenging to devise effective real-time closed-loop active flow control procedures.

In recent years, machine learning has made significant advances, and active flow control is becoming more effective and intelligent (Brunton & Noack 2015). One of the earliest machine learning techniques applied in this field was genetic programming (GP). GP uses a population of computer programs as potential solutions to a problem. The programs evolve using genetic operators like mutation and crossover, and the fittest ones produce the next generation of solutions. Gautier *et al.* (2015) applied GP to search explicit control laws for reducing the recirculation zone behind a backward-facing step. Zhou *et al.* (2020) applied the linear GP to control the dynamics of a turbulent jet and discovered novel wake patterns. Ren *et al.* (2019) adopted GP-identified control laws to successfully suppress vortex-induced vibrations in a numerical simulation environment. Pino *et al.* (2023) demonstrated that many techniques from the ML family can be applied to AFC tasks, from GP to Bayesian Optimization (BO), LIPSchitz global Optimization (LIPO), and Reinforcement Learning (RL), and that these methods have trade-offs relatively to each others.

Artificial neural networks (ANNs) can also be trained to learn complex patterns and relationships in fluid dynamics data and to generate control strategies that optimize fluid manipulation, which can be used for various tasks, including predicting fluid flow patterns, controlling robotic arms that manipulate fluids, and optimizing the design of microfluidic devices. Lee *et al.* (1997) applied an adaptive controller based on a neural network for turbulent channel flow, demonstrating a simple control scheme that reduced skin friction by up to 20% and produced an optimum wall blowing and suction proportional to a local sum of wall-shear stress.

With the rapid development of deep reinforcement learning (DRL), which is effective at interacting with complex nonlinear environments, has brought new ideas to the above flow control problems. Previous studies have shown that deep reinforcement learning can effectively acquire control strategies in high-dimensional, non-linear, and other complex environments. Suppose that deep reinforcement learning is employed to interact with a flow control environment, in such a scenario, it is essential for the closed-loop flow control method to establish the control law based on the learned strategy after continuous trial and error and adjustment of the optimization strategy. For example, Rabault *et al.* (2019) introduced DRL to active flow control for the first time by applying deep reinforcement learning to blunt body drag reduction at $Re = 100$ and successfully demonstrated a closed-

loop active control strategy that could achieve stable drag reduction of about 8% by using proximal strategy optimization (PPO) method. In this study, the velocity measured by 151 sensors located around the cylinder and in the downstream flow field (each sensor collects both the flow lateral velocity) is used as the feedback signal. Besides, Paris *et al.* (2021) employed the S-PPO-CMA method, a novel DRL algorithm, to optimize the sensor position and investigate the efficiency and robustness of the identified control strategy. The algorithm is proposed to optimize the sensor layout and reduce the number of sensors while keeping state-of-the-art performance and successfully acquired a closed-loop active control strategy with stable drag reduction of about 18.4% at $Re = 120$. From a more technical viewpoint, the use of physics-inspired reward functions has been demonstrated by Qin *et al.* (2021), while speedup of the training process was demonstrated using several parallel simulations in Rabault & Kuhnle (2019). In order to investigate higher Reynolds numbers, Ren *et al.* (2021a) applied the Lattice-Boltzmann Method (LBM) to establish a CFD environment with weak turbulence conditions and a Reynolds number of up to 1000 was effectively controlled. Similar to Rabault *et al.* (2019) study, the jet actuators were deployed on the lower and upper sides of the cylinder. The results show that the DRL agent could find an effective feedback law and achieve a drag reduction of more than 30%. Applications in even more chaotic conditions, corresponding to 2D cylinder at a Reynolds number $Re = 2000$, have recently been presented by Varela *et al.* (2022), highlighting that DRL controllers can learn drastically different control laws as the underlying dominating physics are changed. In order to optimize the sensor layout, sensitivity analysis was conducted. In another study, Tang *et al.* (2020) placed four synthetic jets on the lower and upper sides symmetrically for active flow control of the cylinder. In Xu *et al.* (2020)'s study, two small rotating cylinders were placed obliquely behind the main cylinder at a Reynolds number of 240. The rotational speed of the small cylinders was controlled by a DRL agent. This experimental setup aimed to investigate the potential of wake stabilization using DRL-controlled rotating control cylinders. The findings of the study were later confirmed by Fan *et al.* (2020), who experimentally verified the effectiveness and feasibility of this approach. In addition to its application in the field of AFC, researchers have also aimed to utilize DRL approach to achieve other objectives. These objectives include reducing the energy expenditure of the follower (Verma *et al.* 2018; Novati *et al.* 2017), mitigating vortex-induced vibration (Ren *et al.* 2021b; Mei *et al.* 2021; Zheng *et al.* 2021; Ren *et al.* 2019), shape optimization (Garnier *et al.* 2021; Viquerat *et al.* 2021; Li *et al.* 2021), or the control of turbulent channel flows (Guastoni *et al.* 2023). As the field of DRL applications for fluid mechanics is evolving fast, we refer the reader curious of more details to any of the recent reviews on the topic, *i.e.* Vignon *et al.* (2023); Garnier *et al.* (2021).

Most of the aforementioned studies have collected state information using a large number of velocity sensors in the wake region, which poses significant challenges for practical structural flow fields. For instance, in the case of vehicles and high-rise buildings, it would be more convenient and easier to maintain to deploy surface pressure sensors. However, compared to the state in the wake region, the pressure on the surface of the structure may have insufficient characteristic information, making it difficult for the DRL agent to estimate the state of the entire flow field. This will result in typical reinforcement learning methods being unable to learn effective control strategies. Based on the fact, we introduce dynamic feature (DF) lifting approach into deep reinforcement learning and propose the DF-DRL method. In the case of flow around cylinder, this method can significantly enhance the convergence performance of DRL algorithm, enabling it to achieve a drag reduction effect that is almost consistent with the benchmark (147 velocity sensors deployed in the wake region) with a reduction of 99.3% of the sensor quantity.

The novelty and main contribution of the present study are listed as follow:

- A critical and novel enabler is to lift the sensor signals into dynamic features as input to the actor. Dynamic features contain enough information to predict future states. Dynamic data-driven models of wake flows have, for instance, been build from two filtered pressure signals Bourgeois *et al.* (2013) and time derivatives of the lift coefficient Loiseau *et al.* (2018a). Here, time-delay coordinates of surface pressure signals are used Hervé *et al.* (2012). The resulting dynamic feature-based Deep Reinforcement learning (DF-DRL) improves DRL convergence performance, while reduce lift and drag force coefficient under a sparse state space flow. DF-DRL further reduces the drag coefficient by 2.6% compared to the vanilla one.

- A novel and promising DRL method, called dynamic feature-based Deep Reinforcement learning (DF-DRL), is introduced to improve DRL convergence performance, while reduce lift and drag force coefficient under a sparse state space flow. The results show that the tests with DF-DRL approach further reduces the drag coefficient by 2.6% compared to the vanilla one.

- A comprehensive study of the distribution of the pressure sensors is conducted. In contrast to the existing studies on active flow control with deep reinforcement learning, where the sensors are arranged in the wake region, the present study focuses on surface pressure sensors and investigates the number and layout of these sensors in detail. We observe that under active flow control with a low Reynolds number scenario, a single surface pressure sensor can reach excellent control effect, which is comparable with the effect with 147 sensors located in the wake region.

- To validate the robustness of DF-DRL method, two different inflow situations are conducted, including $Re = 500$ and 1000 . The results indicate that even under a much more complicated scenario with higher Reynold number, the DF-DRL agent with sparse surface pressure sensing is capable of controlling the wake development behind a circular cylinder.

In the present study, we utilized the DRLinFluids package (Wang *et al.* 2022) to train a DRL agent and execute interactions. The package leverages Tensorforce (Kuhnle *et al.* 2017) and Tianshou (Weng *et al.* 2022) packages to provide DRL algorithm libraries, and OpenFOAM (Jasak *et al.* 2007) as the CFD interaction environment. Firstly, we compare the performance of vanilla DRL and DF-DRL based plant to a benchmark case study of flow around a circular cylinder with a Reynolds number of 100. Subsequently, we varied the number of pressure surface sensors to validate the effectiveness of the proposed method. Finally, we trained a DF-DRL agent with a single surface pressure sensor and deployed it to the flow under higher Reynolds numbers of $Re = 500$ and 1000 to illustrate the robustness of the approach.

2. Active flow control system with DRL-based jet actuators

The present section is partitioned into two components: (1) an illustration of the DRL algorithm, especially for the Soft Actor-Critic (SAC) method, which will be used as the DRL part in the whole study; (2) a detailed introduction of the dynamic feature-based DRL framework, including the dynamic feature lifting and the coupling with the flow simulation.

2.1. Deep reinforcement learning

Deep reinforcement learning (DRL) is a powerful method of optimal control based on a parameterized policy, commonly referred to as an agent, that learns through trial and error. In the context of computational fluid dynamics (CFD), the environment can be modeled as the flow over a circular cylinder. During the optimization procedure, the DRL agent interacts with this environment to generate experiences according to the current policy. These experiences are then cached in a buffer and used by the training algorithm to improve

the policy. This iterative process is repeated until the agent can yield a control strategy that satisfies the desired performance criteria. Thus, DRL has the potential to revolutionize the field of fluid mechanics by enabling the discovery of previously unknown control strategies that can enhance the performance of fluid systems.

There are several types of DRL algorithms (François-Lavet *et al.* 2018). One of the most popular types of DRL algorithms is Q-learning (Mnih *et al.* 2013; Bellemare *et al.* 2017; Andrychowicz *et al.* 2018), which uses a neural network to approximate the optimal action-value function, and updates the network’s weights using the Bellman equation to minimize the difference between the predicted and actual reward. Another type of algorithm is policy gradient methods (Mnih *et al.* 2016; Schulman *et al.* 2017b,a), which directly optimize the agent’s policy to maximize the expected reward, and often use techniques like Monte Carlo sampling or trust region optimization. Actor-critic methods (Lillicrap *et al.* 2019; Fujimoto *et al.* 2018; Haarnoja *et al.* 2018) combine the advantages of both Q-learning and policy gradient methods by simultaneously learning a value function and a policy. Another type of DRL algorithm is model-based reinforcement learning (Ha & Schmidhuber 2018; Weber *et al.* 2018; Silver *et al.* 2017), which involves learning a model of the environment dynamics and using it to plan actions. Model-based algorithms can be more sample-efficient than model-free algorithms like Q-learning, but require additional computational resources to learn and maintain the model. Referring to our previous work (Wang *et al.* 2022), the SAC algorithm is a feasible choice and is selected in the following study.

The Soft Actor-Critic (SAC) method (Haarnoja *et al.* 2018) is an actor-critic off-policy DRL algorithm that learns by leveraging a maximum entropy reinforcement learning algorithm. The agent’s goal is to maximize entropy and prospective reward and reach the desired value while acting as randomly as possible. Since it is an off-policy algorithm, training can be performed efficiently with limited samples. The optimal policy can be formulated as

$$\pi^* = \arg \max_{\pi(\theta)} \mathbb{E}_{(s_t, a_t) \sim \rho_\pi} \left[\underbrace{\sum_t R(s_t, a_t)}_{\text{Reward}} + \alpha \underbrace{H(\pi_\theta(\cdot | s_t))}_{\text{Entropy}} \right], \quad (2.1)$$

$$H(\pi_\theta(\cdot | s_t)) = - \sum_{i=1}^n p(\pi_\theta(\cdot | s_t)) \log p(\pi_\theta(\cdot | s_t)), \quad (2.2)$$

where $R(s_t, a_t)$ represents the reward for taking action a_t in state s_t , $H(\pi_\theta(\cdot | s_t))$ is the entropy of the policy π_θ at state s_t , and α is the temperature coefficient. The smaller α is, the more uniform the distribution of the output action becomes, and the maximum entropy reinforcement learning degrades to standard reinforcement learning (i.e., $\alpha \rightarrow 0$). The objective is to find the optimal policy π_θ that maximizes the expected reward while also maximizing entropy.

The core idea behind the maximum entropy approach is to randomize the policy by distributing the probability of each action output widely, rather than concentrating on a single action. This approach enables the neural network to explore all possible optimal paths and avoid losing the essence of maximum entropy to a single action or trajectory. The resulting benefits include the following: (1) Learning policies that can serve as initializations for more complex tasks, as the policy learns multiple ways to solve a given task, making it more conducive to learning new tasks. (2) Strengthening the ability to explore, which makes it easier to identify better patterns under multimodal reward conditions. (3) Enhancing the robustness and generalization ability of the approach since the optimal possibilities are explored in different ways, making it easier to adjust in the presence of interference.

The entropy term in the SAC algorithm affects the policy’s exploration in two important ways. First, the entropy term encourages the policy to take more exploratory actions by

adding a penalty to the objective function for actions that have low probability under the current policy. This penalty is proportional to the negative entropy of the policy, which measures the degree of randomness or uncertainty in the actions selected by the policy. By minimizing this penalty, the policy is incentivized to explore more widely and try out new actions that may lead to higher rewards. Second, the entropy term also helps prevent the policy from becoming too deterministic, which can limit its ability to adapt to changes in the environment or learn new behaviors. By adding an entropy term to the objective function, SAC encourages the policy to maintain a balance between exploration and exploitation, rather than becoming overly focused on a single optimal action. This can be particularly important in environments with multiple suboptimal solutions or where the optimal solution may change over time. In summary, the entropy term in SAC encourages exploration by penalizing the policy for taking low-probability actions, and helps prevent the policy from becoming too deterministic by promoting a balance between exploration and exploitation. This can lead to better performance and more robust learning in complex, dynamic environments.

The SAC algorithm used in this study employs a maximum entropy target as its optimization objective, which has been shown to enhance the algorithm’s exploration properties and robustness. The ability to effectively explore is achieved by maximizing information entropy, which promotes a uniform distribution of the probability of each action output, rather than focusing on a single action. For instance, the Uniform strategy is a high-entropy strategy. On the other hand, the robustness of the algorithm is reflected in its ability to generate alternative action outputs when faced with environmental noise. In contrast, a previous greedy strategy may lead to the agent’s inefficacy due to the certainty of its actions. The SAC algorithm ensures that every action has a varying probability, rather than being either high or low. Therefore, when the environment encounters noise, the agent can still produce alternative action outputs without failure. From these perspectives, the SAC algorithm is highly suitable for the present study, which involves the application of active flow control (AFC) using surface pressure temporal series. For a more detailed description of the SAC algorithm, please refer to Haarnoja *et al.* (2018).

The present work employs a closed-loop control framework for the AFC task described in Sec. 3.2, as depicted in Fig. 1. The framework comprises two main components: the environment and the DRL agent (critic and actor in the case of the SAC algorithm used). The flow around a circular cylinder is simulated by OpenFOAM as has been described in Sec. 3.2. The flow velocity or pressure measured by specific sensors is collected as the state provided to the agent. Following the setup of sensors in Rabault *et al.* (2019)’s study, a total of 147 sensors can capture sufficient flow information for control policy learning, which is adapted as a baseline. The DRLinFluids package (Wang *et al.* 2022) is used to accomplish the interaction between the DRL agent and the CFD simulation, and Tianshou (Weng *et al.* 2022) is employed as the DRL algorithm backend. The DRL policy network consisting of two dense layers, each with 512 fully connected neurons. The input layer receives data from pressure sensors, and the output layer gives the jet velocity. The time interval between each step is set to 7.5% of the vortex-shedding period of the cylinder without actuators. The SAC agent interacts with and updates the ANN parameters every 50 steps. The process is repeated three times with the same hyperparameters to ensure the stability and validity of the training. To save training time and provide a consistent start point, a vanilla case without control is simulated in advance until reach a stable status, then the state of the flow field is stored and utilized as the initialization for the following DRL training stage.

To avoid non-physical abrupt changes in pressure and velocity resulting from the use of incompressible CFD algorithms, a continuous-time approach is adopted for the control mechanism. The control for each jet is determined at every time step during the simulation and smoothed to obtain a continuous control signal over time. An appropriate interpolation

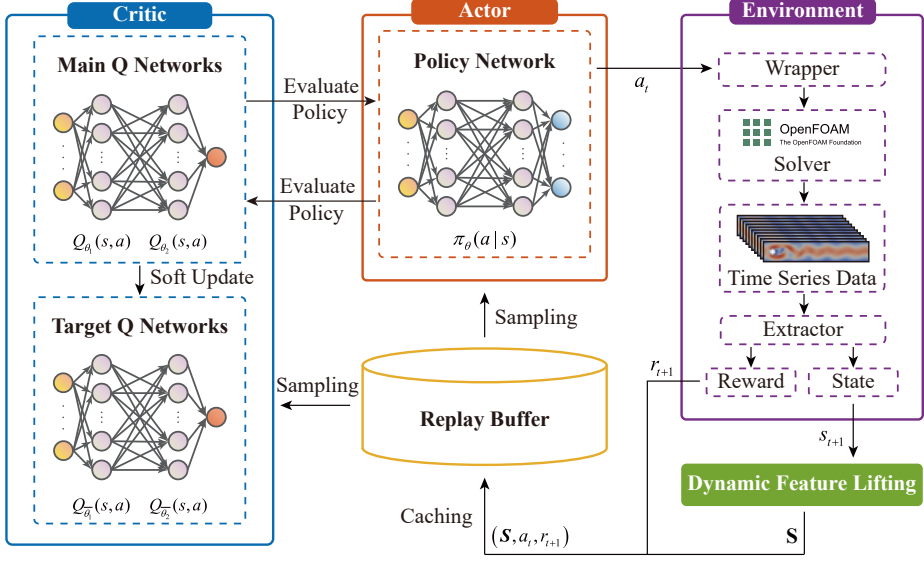


Figure 1: Schematic of the DF-DRL(SAC) framework used in the present study. The term *wrapper* refers to the process of encapsulating actions from the agent and sending it to OpenFOAM solver, while *extractor* refers to the process of parsing CFD results and providing feedback to the agent. This entire framework is derived from the DRLinFluids package (Wang *et al.* 2022).

method is crucial to serialize the received time-discretized control signal for this system. Hence, we smooth the jet actuation to ensure a continuous change in the control signal without excessive lift fluctuations due to sudden changes in jet velocity. Based on the interpolation functions demonstrated by Tang(Tang *et al.* 2020), the control action is set to change linearly as follows:

$$V_{\Gamma_i}(t) = V_{\Gamma_i}(t-1) + [a - a_{(t-1)}]/N_e, \quad i = 1, 2, \quad (2.3)$$

where $V_{\Gamma_i}(t)$ and $V_{\Gamma_i}(t-1)$ is the jet flow velocity used at the non-dimensional times t and $t-1$ respectively, and a is the flow velocity of jet Γ_i for the current 50-time steps, *i.e.* the action generated by the DRL agent.

Flow control of circular cylinders is a highly popular topic in both academic and industrial sectors. The aim of this research is to reduce or eliminate drag and lift forces, using advanced reinforcement learning techniques. This objective can be achieved by setting an appropriate reward function. A reward function that combines drag and lift coefficients is proposed to achieve the optimization goal, which is set as follows:

$$R_t = (C_D)_{Baseline} - \langle C_D^t \rangle_T - 0.1 * |\langle C_L^t \rangle_T|, \quad (2.4)$$

where $(C_D)_{Baseline}$ is the mean drag coefficient of the circular cylinder without flow control, C_D^t and C_L^t means temporal drag and lift coefficient at the time t respectively, and $\langle \cdot \rangle_T$ indicates the sliding average back in time over a duration corresponding to one jet flow control period T with active flow control.

2.2. Active flow control with dynamic feature-based DRL enhancement

For DRL tasks, the agent needs to perceive the state of the environment and give corresponding actions. Deep reinforcement learning has long emphasized setting an appropriate reward function while ignoring the modeling of the environmental state. This may be related to different types of learning tasks. For example, in the fields of robotics (Nguyen & La 2019)

or autonomous driving (Kiran *et al.* 2022), DRL state almost invariably selects temporal image sequences as inputs and is assisted by commonly used feature extraction techniques such as Convolutional Neural Network (CNN) and Long Short-Term Memory (LSTM). However, in the field of flow control, especially for various structural drag reduction tasks (such as vehicles and high-rise buildings) in the real world, it is often difficult to observe or model information on the velocity or pressure of the entire flow field with respect to the complex dynamic system, which makes the perception of environmental state itself a challenge. Further, this problem can be formulated as how to estimate information on the full flow field through fewer sensor data. This is actually regard as pattern recognition and reduced order modelling, which have always been hot topics in the field of fluid mechanics research.

CFD numerical simulations provide the opportunity to collect space-time-resolved data within the considered computational domain. However, in the real world, it is often difficult to obtain a comprehensive view of the flow field, which means only a limited number of time-resolved sensor measurements s are accessible. The objective of this study is to demonstrate how recent advancements in system identification and machine learning can be utilized to construct reduced-order models directly from these sparse sensor measurements. To achieve this, we simulate experimental conditions using direct numerical simulations, and focus on a single sensor measurement represented by

$$s(t) := p(t; \mathcal{L}), \quad (2.5)$$

where p is the surface pressure. The measurement vector s , generally, can comprise various measurements such as the lift and drag coefficients, pressure measurements on a cylinder, or velocity field measurements at specific locations, e.g., wake region. However, for the scope of this study, the pressure alone is deemed adequate to characterize the flow according to the results shown in §4.1.

Given the sensor measurements s , our objective is to develop an effective flow state estimation that enables a DRL agent can obtain efficient information based on it. However, raw signals may not be ideal for the purposes, and an augmentation or dynamic feature lifting is required with incorporating sensor measurement functions. In this regard, we define the augmented state S as a feature vector that encompasses such functions:

$$S = g(s) \quad (2.6)$$

There exist numerous options for the mapping function g , which can enhance sensor measurements and improve model accuracy. If the sensors are adequate to determine the system state, the identity map can be utilized as g , which means $S = s$. Alternatively, when the measurements provide high-dimensional snapshots, g can leverage Proper Orthogonal Decomposition (POD) mode coefficients. Takens (1981) and Brunton *et al.* (2017) use delay embedding technology to augment the measurements, resulting in a sufficiently high-dimensional feature vector that fully characterizes the system dynamics. The task of selecting an effective transformation function g is a critical unresolved issue that is relevant to both representation theory and the Koopman operator viewpoint on dynamical systems. Both Mezić (2005) and Brunton *et al.* (2016a) are actively engaged in investigating this problem. In this study, we choose g to augment the sensor measurement with its time derivative, while appropriately scaling the augmented measurement. Furthermore, Loiseau *et al.* (2018b) propose a comprehensive sparse reduced-order modelling for flow full-state estimation, which includes time-resolved sensor data and optional non-time-resolved particle image velocimetry (PIV) snapshots.

Inspired by the aforementioned facts, we presents a novel approach, named dynamic feature-based DRL, to overcoming the limitations of measurements in real world and

highlights the potential of deep reinforcement learning techniques for sparse surface pressure sensing. An effective augmentation function \mathbf{g} at time t is used to lift the sensor signals so that a high-dimensional dynamic feature space is formed, which can be expressed as

$$\mathbf{S}_t = \begin{pmatrix} \alpha s_1^{t-M} & \cdots & \alpha s_i^{t-M} & \beta a_1^{t-M} & \cdots & \beta a_j^{t-M} \\ \vdots & \ddots & \vdots & \vdots & \ddots & \vdots \\ \alpha s_1^t & \cdots & \alpha s_i^t & \beta a_1^t & \cdots & \beta a_j^t \end{pmatrix} \in \mathbb{R}^{(M+1) \times (i+j)}, \quad (2.7)$$

where a is the agent action at time t , M is the number of backtracking time steps, which is set to 30 in this study, i and j are the identifier of sensor and actuator, respectively, α and β are corresponding scaling factor.

In past studies, a common practice has been to use a single snapshot of the flow field as state data, such as four sensors of pressure data in one time step, to provide as input to the policy network. This is illustrated by the upper panel of Fig. 2. By contrast, the DF-DRL method uses pressure data assembled from sensor measurements extracted from the 30 previous action time steps, resulting in an augmented agent state. The details of dynamic feature lifting within DF-DRL method is illustrated in lower Fig. 2. It is expected (and, in fact, confirmed in §4.1) that the policy will be improved using such dynamic feature lifting input data. However, a possible challenge is that this may increase quite a bit the dimensionality of the state input to the ANN, since it is a two-dimensional array with one dimension corresponding to the sensor number, and another dimension corresponding to the timeseries index. In particular, sensors on the surface observe lower magnitude variations in flow velocity and pressure than sensors in the wake, and are unable to observe changes in the trend of the wake and the shedding of cylinder vortices. Therefore, using the DF-DRL method is most appropriate for the surface sensors AFC training process, which involves fewer sensors. Besides, it is also vital to use an input standardization method individually on each sensing time series. In particular, it is necessary to normalize the surface pressure sensors observations so that these fluctuations are well perceived even though these have a very different dynamic range compared with sensors in the wake region.

3. Numerical plant: laminar flow around circular cylinder

In this paper, we choose the classic benchmark proposed by Schäfer *et al.* (1996), laminar flow around a cylinder, and place jets symmetrically arranged on both lateral sides as actuators for active flow control. The objective is to reduce the drag force and lift fluctuation on the cylinder. Firstly, we formalize the research problem in §3.1. Then, we provide a detailed description of the flow configuration and numerical solution methods in §3.2, followed by a validation of the accuracy of the numerical algorithms. Finally, we define three different types of sensor installation methods in §3.3.

3.1. Problem formalization

The active flow control task formulated in this study aims at finding out a real-time control policy π of two jet actuators located on a circular cylinder with sensor feedback, which can effectively reduce the fluid force on it. Generally, the surface pressure information s_t can be regarded as the input state of the control policy π , and the jet intensity can be viewed as the DRL action a_t at the time t . The action is decided by the DRL controller based on the state observation. Therefore, the control processing can be modeled as a deterministic or stochastic relationship:

$$a_t \sim \pi(s_t|\theta). \quad (3.1)$$

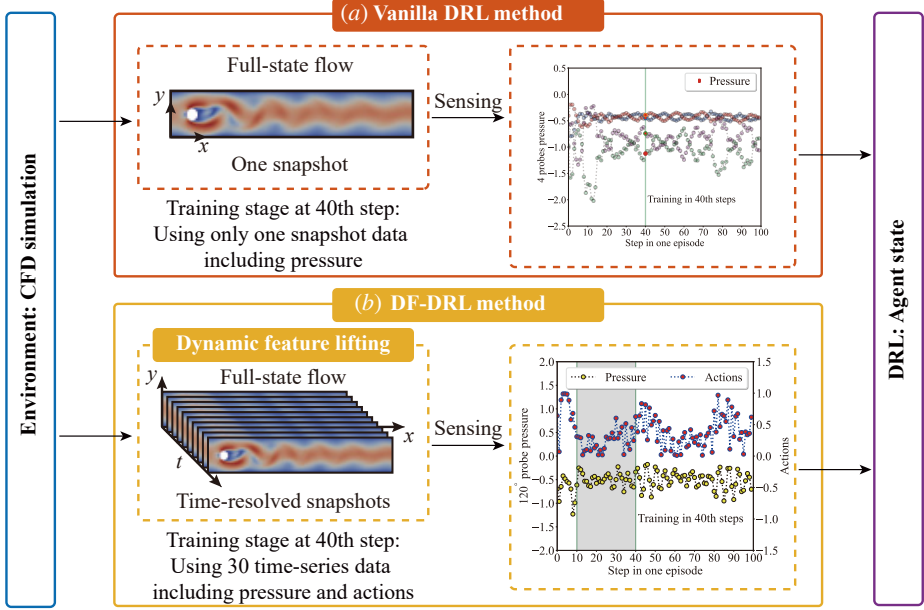


Figure 2: Flowchart of the two approaches for the state collected from the environment.

(a) Vanilla method (Sensor-feedback): the agent only collects the flow field state at a single time step. For example, the signal obtained from four pressure sensors located in the flow field at the 40th time step return a state vector $s \in \mathbb{R}^{4 \times 1}$; (b) DF-DRL method: the agent collects data from the most recent thirty time steps, including historical sensor pressure $p \in \mathbb{R}^{30 \times 1}$ and action data $a \in \mathbb{R}^{30 \times 1}$ provided by the agent. This process indicates dynamic feature lifting, and the dimension of the state vector $S \in \mathbb{R}^{30 \times 2}$. Moreover, scaling the state vector will amplify signal fluctuations, which is helpful to capture the flow characteristics.

Hence, given a deep reinforcement learning agent with the control policy π , the objective is to minimize the lift and drag coefficients of the cylinder by optimizing the set of weights θ of the DRL agent policy network:

$$\pi^* = \pi(\theta^*), \quad (3.2)$$

$$\theta^* = \arg \max_{\pi(\theta)} \mathbb{E}_{(s_t, a_t) \sim \rho_{\pi(\theta)}} \mathcal{T}(s_t, a_t), \quad (3.3)$$

where the superscript $*$ represents the optimal value, \mathbb{E} is the expected value operator, and \mathcal{T} denotes a target function, which represents the current policy π .

3.2. Flow configuration and numerical method

In this work, we use the open-source computational fluid dynamics software package OpenFOAM (Open-source Field Operation And Manipulation) developed by the OpenFOAM Foundation to perform simulations. Under the assumption of incompressible viscous flow, the governing Navier-Stokes equations can be expressed in a non-dimensional manner as:

$$\frac{\partial \mathbf{u}}{\partial t} + \mathbf{u} \cdot (\nabla \mathbf{u}) = -\nabla p + Re^{-1} \Delta \mathbf{u}, \quad (3.4)$$

$$\nabla \cdot \mathbf{u} = 0, \quad (3.5)$$

$$Re = \frac{\bar{U}D}{\nu}, \quad (3.6)$$

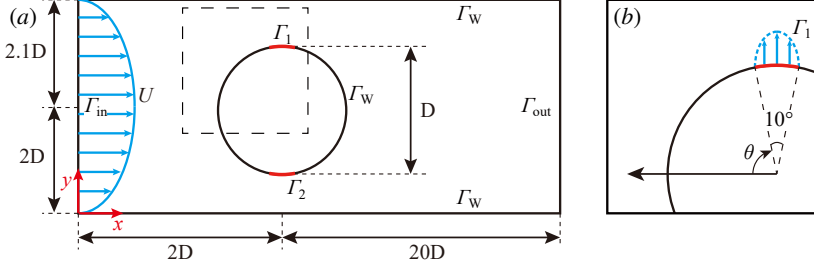


Figure 3: Description of (a) the numerical setup, which is adapted from Schäfer *et al.* (1996). The origin of the coordinates is located at the lower left corner of the entire computational domain. Γ_{in} stands the inflow velocity with a parabolic flow profile, while Γ_{out} is put for the outflow. Non-slip wall boundary constraint Γ_w is applied on the bottom and top of the channel, as well as on the cylinder surfaces. Two jet holes (Γ_1 and Γ_2) are present at both sides of the cylinder; (b) An enlarged view of the dashed box in subfigure (a). The 0° azimuth angle is corresponding to the foremost point on the cylinder's windward surface, and increases in a clockwise direction. The jet actuator opening angle is 10° , consistent with Rabault *et al.* (2019).

where \mathbf{u} is the non-dimensional velocity, t is the non-dimensional time, p is the non-dimensional pressure, ν is the kinematic viscosity of the fluid, and \bar{U} is the mean velocity at the inlet. The corresponding Reynolds number Re is 100 in the training stage.

This study focuses on two-dimensional simulations of flow around a circular cylinder with a diameter D , which is the characteristic length scale. The computational domain has dimensions of $L = 22D$ and $B = 4.1D$ in the streamwise and cross-stream directions, respectively, as shown in Fig. 3. Following the widely recognized benchmark conducted by Schäfer *et al.* (1996), the cylinder is slightly off-center to induce faster development of the vortex shedding alley during the initial simulation convergence stage. The outlet boundary is placed $19.5D$ downstream of the cylinder to allow the wake to fully develop.

The inlet boundary denoted as Γ_{in} is subject to the parabolic velocity inlet boundary condition. The no-slip constraint, Γ_w , is applied to both the top and bottom of the channel and the surfaces of the cylinder. Additionally, the right boundary of the channel, Γ_{out} , is designated as a pressure outlet, wherein zero velocity gradient and constant pressure are maintained. The inlet boundary is assigned as a parabolic velocity form and expressed as the following in the streamwise direction:

$$U(0, y) = 4U_m y(H - y)/H^2, \quad (3.7)$$

where U_m is the maximum inflow velocity at the middle of the channel. Employing a parabolic inflow profile, U_m is 1.5 times the mean velocity \bar{U} , as defined by:

$$\bar{U} = \frac{1}{H} \int_0^H U(y) dy = \frac{2}{3} U_m. \quad (3.8)$$

To accomplish the active flow control, the flow control technique using two jet actuators (Γ_1 and Γ_2) located on opposite sides of the cylinder is employed. A parabolic velocity profile with a jet width of $\omega = 10^\circ$ is imposed at both jets, as depicted in Fig. 3. Due to the velocity of the jet flow being orthogonal to the inflow direction, drag reduction is strictly achieved by effective actuation rather than by momentum injection. Moreover, the jet flow on both sides is constrained as synthetic jet flow, i.e., $V_{\Gamma_1} = V_{\Gamma_2}$, so that the jets collectively do not add nor remove mass to the flow.

In the current study, unstructured meshes are adopted for computational fluid dynamics (CFD) simulations. Emphasis has been laid on refining the mesh around the surface boundary

Table 1: Numerical results of mesh convergence study for the 2D flow around a circular cylinder at $Re = 100$.

Case	Grid number	C_D^{\max}	C_L^{\max}	$\overline{C_D}$	St
Grid I	13572	3.27	1.01	3.21	0.301
Grid II	16200	3.24	1.024	3.205	0.299
Grid III	39382	3.24	1.04	3.21	0.302
Schäfer <i>et al.</i> (1996)		3.22-3.24	0.99-1.01		0.295-0.305
Rabault <i>et al.</i> (2019)	9262	3.245	1.020		0.302

and the wake flow regions, as these are crucial for ensuring the appropriate resolution of these significant flow domains and of the physics happening there. The numerical solution is obtained at each time step, and the drag (F_D) and lift (F_L) forces are computed by integrating over the cylinder surface, following:

$$\mathbf{F} = \int (\boldsymbol{\sigma} \cdot \mathbf{n}) \cdot \mathbf{e}_j \, d, \quad (3.9)$$

where $\boldsymbol{\sigma}$ is the Cauchy stress tensor, the unit vector \mathbf{n} is defined as normal to the cylinder surface, while \mathbf{e}_j is denoted as a unit vector in the direction of the inflow velocity for drag force calculations, and as a vector perpendicular to the inflow velocity for lift force calculations. Specifically, the drag C_D and lift C_L coefficients can be expressed as follows:

$$C_D = \frac{F_D}{\frac{1}{2}\rho\bar{U}^2D}, \quad (3.10)$$

$$C_L = \frac{F_L}{\frac{1}{2}\rho\bar{U}^2D}, \quad (3.11)$$

where F_D and F_L are denoted as integral drag and lift force, respectively.

To further validate the accuracy of the CFD simulations, a series of mesh convergence studies are performed at a Reynolds number $Re = 100$. In particular, meshes of three different resolutions are employed, and the corresponding results for the maximum values of the drag coefficient C_D and lift coefficient C_L , denoted as C_D^{\max} and C_L^{\max} , respectively, are reported in Table 1. The numerical analysis reveals that the discrepancies among various mesh resolutions are insignificant. Considering the trade-off between computational cost and numerical accuracy, the meshing scheme of Grid II is preferred for the DRL training stage.

3.3. Layout of surface pressure sensors

In the present study, a series of pressure sensor layout schemes are proposed to study the influence of sensors location. First, a baseline configuration proposed by Rabault *et al.* (2019) with 147 pressure sensors are set up both around the cylinder and in the wake region, as shown in Fig. 4(a). Then, A varying number of pressure sensors, e.g. 4, 8, 24 sensors, are symmetrically arranged on the surface of the cylinder (along the direction of inflow). To avoid the inadequate information with smaller pressure fluctuations at the front of the cylinder, the sensors are uniformly distributed with the exception of the point at the front, as shown in Fig. 4(b). Finally, a comprehensive study is carried out using a single sensor location. The placement of the single sensor is started putting it at the front of the cylinder as $\theta = 0^\circ$ relatively to the incoming flow, and we change its position by gradually increasing its angular position on the cylinder in increments of 15° until it reaches the rear edge of

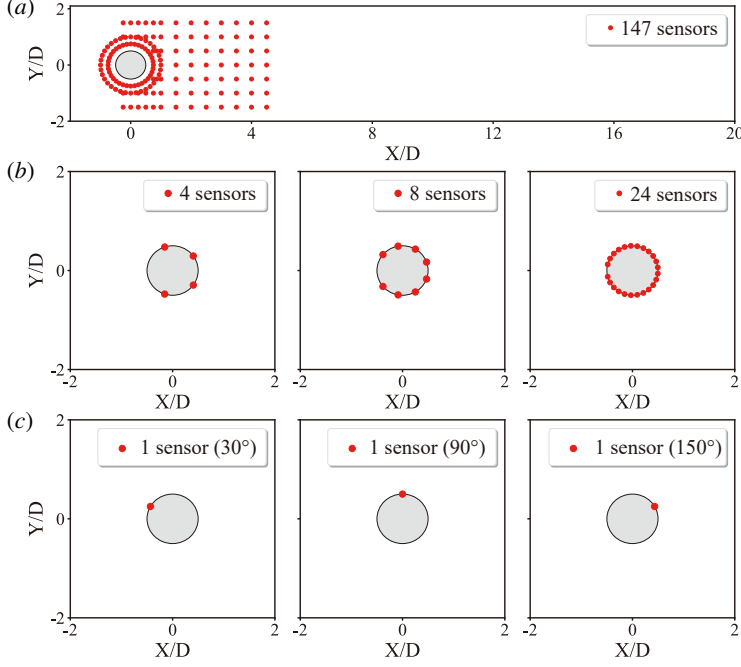


Figure 4: Number and configuration of the sensors used to generate the DRL controller state observation: (a) Using 147 sensors provides sufficient flow information for DRL training; (b) Layout using 4, 8 and 24 sensors in the surface of the cylinder respectively; (c) Layout using only one sensor located on the surface of the cylinder with azimuth angle of 30° , 90° and 150° .

the cylinder ($\theta = 180^\circ$), as shown in Fig. 3(c) and Fig. 4(c). As a consequence, a total of 17 single pressure sensor positions are investigated. One could expect that pressure sensors on the surface of the cylinder can provide valuable information about the flow to the DRL controller. However, using surface sensors like those shown in Fig. 4(b) and (c) presents a challenge due to limited quantity of data provided and the placement being solely on the surface of the cylinder. This results in a lack of information regarding the cylinder wake and vortex shedding pattern during the DRL training stage.

In order to facilitate the description in the next sections, the notation \mathcal{L} is used to describe the different sensor layout schemes. The subscripts represent different sensor layout types, for example, \mathcal{L}_I represents the baseline configuration with 147 sensors placed inside the flow field, \mathcal{L}_{II} represents the sensor configuration placed on the cylinder surface, and \mathcal{L}_{III} represents a single sensor configuration placed on the cylinder surface. For type \mathcal{L}_{II}^N , the superscript N indicates the number of sensors, and the polar coordinates of sensor i can be expressed as

$$r_i = \frac{1}{2}D, \quad \theta_i = \frac{2\pi i}{N+1}, \quad i = 1, 2, \dots, N, \quad (3.12)$$

while for type \mathcal{L}_{III}^θ , the superscript θ indicates the angle of the sensor placement where the coordinate axis of the polar coordinate system with origin opposite to the inflow direction, *i.e.*, the leading edge of the cylinder is denoted as the 0° point, which is illustrated in Figure 4.

4. Results and discussion

In this section, we first evaluate the performance and reliability of the proposed DF-DRL approach in §4.1, comparing with a vanilla DRL algorithm. Then, the impact of different number of surface sensors configurations and layouts of single surface sensors on the performance of flow control are investigated in §4.2. Furthermore, we verify the robustness of the DF-DRL controllers under two different Reynolds numbers, $Re = 500$ and $Re = 1000$ in §4.3.

4.1. DRL-based AFC with sparse surface pressure sensing

To evaluate the effectiveness and reliability of the DF-DRL approach, sensor locations \mathcal{L}_I and \mathcal{L}_{II}^4 are selected for illustration, as depicted in Fig. 4(a) and (b), respectively. Figure 5 shows the learning curves for active flow control using both vanilla DRL and DF-DRL techniques under two different sensor quantity configurations (4 and 147 sensors). The three subplots (a), (b), and (c) correspond to the mean drag coefficient, reward, and the standard deviation (std) of lift coefficient, respectively.

The results indicate that there are significant differences between these four cases. Using a vanilla DRL algorithm, the maximum drag reduction of 8% was achieved with the use of 147 sensors (scheme \mathcal{L}_I), and the maximum reward value is 19.13. Moreover, the standard deviation of the lift coefficient is reduced to 0.15 when learning has converged. For the case of 4 sensors with vanilla DRL method (scheme \mathcal{L}_{II}^4), the maximum drag reduction is only 6.4%, and the std of the lift coefficient decreases to only 0.29, as shown in Fig. 5. These two cases show that with few surface sensors, the performance of active flow control performance becomes worse. This is due to the inability of DRL to correctly estimate the flow field and limited observable data.

As for the results using the DF-DRL method, it is observed that both \mathcal{L}_I and \mathcal{L}_{II}^4 achieve similar drag reduction amplitudes of 8%, corresponding to the maximum drag reduction also observed using the 147 pressure sensors. However, the latter approach achieves a higher reward value, as indicated by the decrease in the standard deviation of the lift coefficient due to the lift penalty term within the reward function. This improvement in performance is happening despite the fact that both the \mathcal{L}_I and \mathcal{L}_{II}^4 approaches undergo a temporary rebound in their learning. Therefore, when utilizing DF-DRL method, fewer sensors, as used in scheme \mathcal{L}_{II}^4 , can achieve the same drag reduction as scheme \mathcal{L}_I which achieve 25% better than the vanilla model based on direct sensor-feedback. This can be obtained while also improving on the reduction of lift fluctuations. These observations suggest that the DF-DRL method can maintain drag-reduction performance while reducing the number of sensors required. The difference in reward observed between the two cases can be attributed to the reduction in the standard deviation of the lift coefficient achieved in scheme \mathcal{L}_{II}^4 .

For scheme \mathcal{L}_I , with a large number of sensors distributed around the cylinder and wake region, the DRL controller is able to obtain exhaustive flow field information, and thus the inclusion of historical data provided by the DF-DRL method has a minor impact. However, for scheme \mathcal{L}_{II}^4 , with limited sensor numbers and sparse information on the cylinder surface, without the DF-DRL method, there is not enough information available to perform effective flow control. These results suggest, unsurprisingly, that the use of more sensors leads to better drag coefficient reduction effects and more stable reward convergence with naive DRL agent. Moreover, when the flow field information is limited in quantity and placement of the sensors (due to physical restrictions), the DF-DRL method demonstrates better convergence and yields a superior control policy.

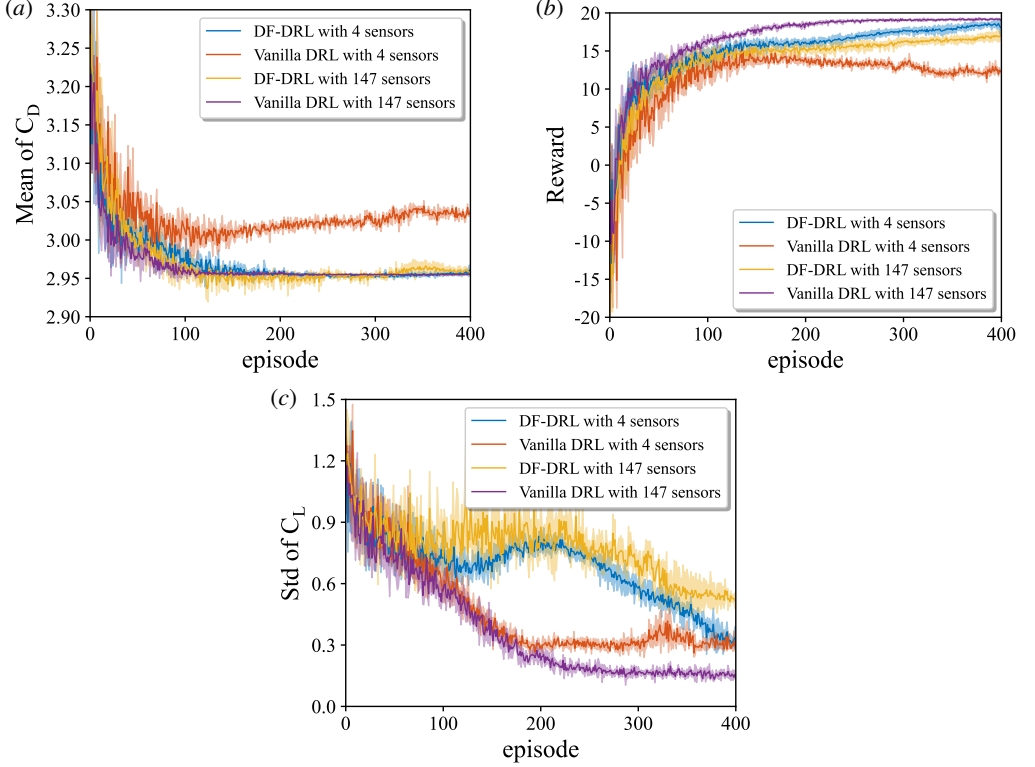


Figure 5: Comparison of (a) mean drag coefficient C_D , (b) reward, and (c) std of lift coefficient when using different DRL methods, *i.e.*, using the DF-DRL method or not, and different number of sensor (4 sensors in the surface of cylinder and 147 sensors around the cylinder). The learning case condition which contains 147 sensors and without time series, reaches the maximum reward. All of these cases are trained three times repeatedly, and we present the average between the 3 runs (thick line) and the standard deviation between these runs (shadowed area).

4.2. Control performance and learning convergence with DF-DRL method

To further investigate the impact of sensor quantity and placement azimuth on the control effectiveness and convergence performance of the DF-DRL based controller, we conducted case studies with different quantities of sensor, *i.e.*, 1, 4, 8, 12, 24, and 36, as well as various placement azimuth layouts of 0° to 180° with a 15° spacing.

4.2.1. Sensor quantity

Five typical layout schemes \mathcal{L}_{II} of surface pressure sensors are investigated in this section. The arrangement of these sensors is depicted in Fig. 4(b), where the sensors are evenly distributed and all the leading edge sensor is removed, as described in 3.3. Since the state includes the jet actions component, the pressure sensors distributed around the jet will not significantly impact the results.

The impact of adding more surface pressure sensors on training performance is illustrated in Fig. 6. Results show that increasing the number of sensors does not lead to a significant improvement in drag and lift coefficient reduction, which remains around 8% across all schemes. Additionally, all cases converge at approximately 200 episodes. Figure 6(b) displays learning curves that follow the same trend as the drag coefficient, indicating that the final

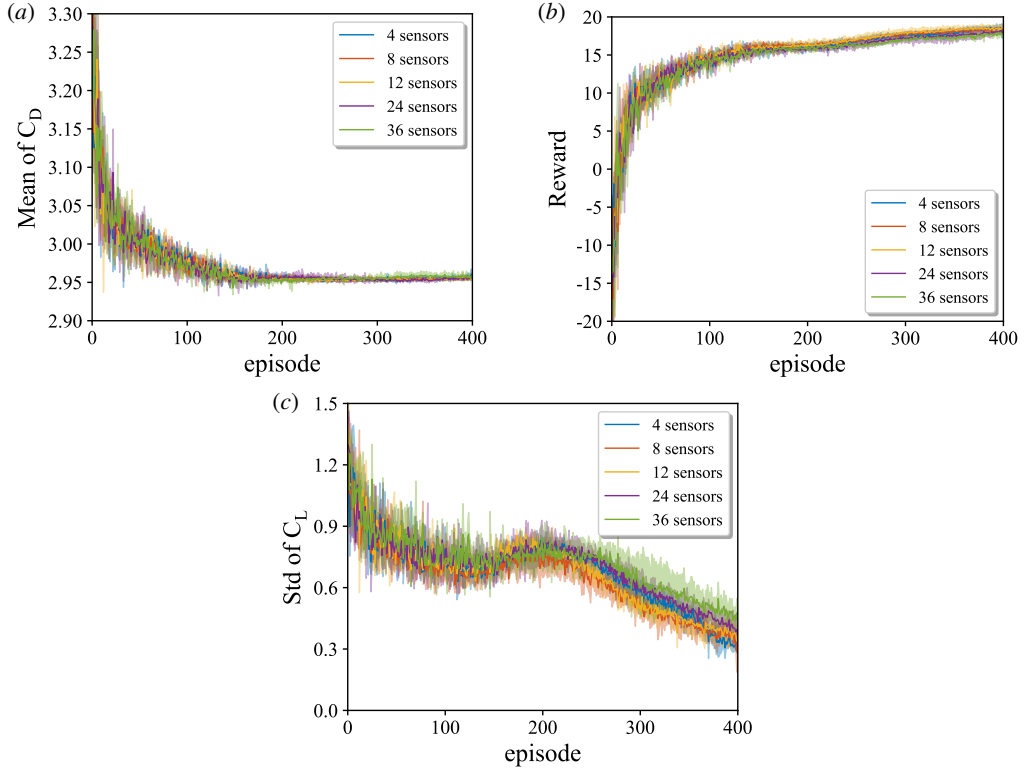


Figure 6: Evolution of (a) mean drag coefficient reduction C_D , (b) reward and (c) std lift coefficient in different number of sensor with DF-DRL method. Sensors are uniformly located on the surface of the cylinder as indicated in Fig. 4(c).

DF-DRL performance is very similar to the benchmark case for different numbers of pressure sensors on the surface of the cylinder.

As depicted in Fig. 6(c), the standard deviation of the lift exhibits a comparable declining pattern to that observed in the previous section. Following an initial decrease and temporary increase at around episode 200, all five groups undergo a consistent decrease until the completion of DF-DRL training.

This result can be explained by the fact that the pressure on the cylinder surface, as a surrogate for lift, is a better dynamic feature than wake measurements, where varying vortex shedding destroys the phase relationship. The pressure on the cylinder surface provides a more accurate representation of the dynamic behavior of the flow, leading to a better understanding of the underlying physics. This conclusion is in agreement with previous work by Loiseau *et al.* (2018b). The use of pressure as a dynamic feature highlights the potential for feature-based approaches in reduced-order modeling of fluid flows. Given that the disparities in drag coefficient and lift fluctuation reduction among the experiments are not substantial, to further demonstrate the potential of using surface pressure as a dynamic feature for nonlinear system and its combination with DRL, we will reduce the number of sensors to one in the next section.

4.2.2. Placement azimuth

Based on the results above, it is apparent that an increase in the number of sensor utilized in DF-DRL based AFC task does not necessarily result in better performance, including drag

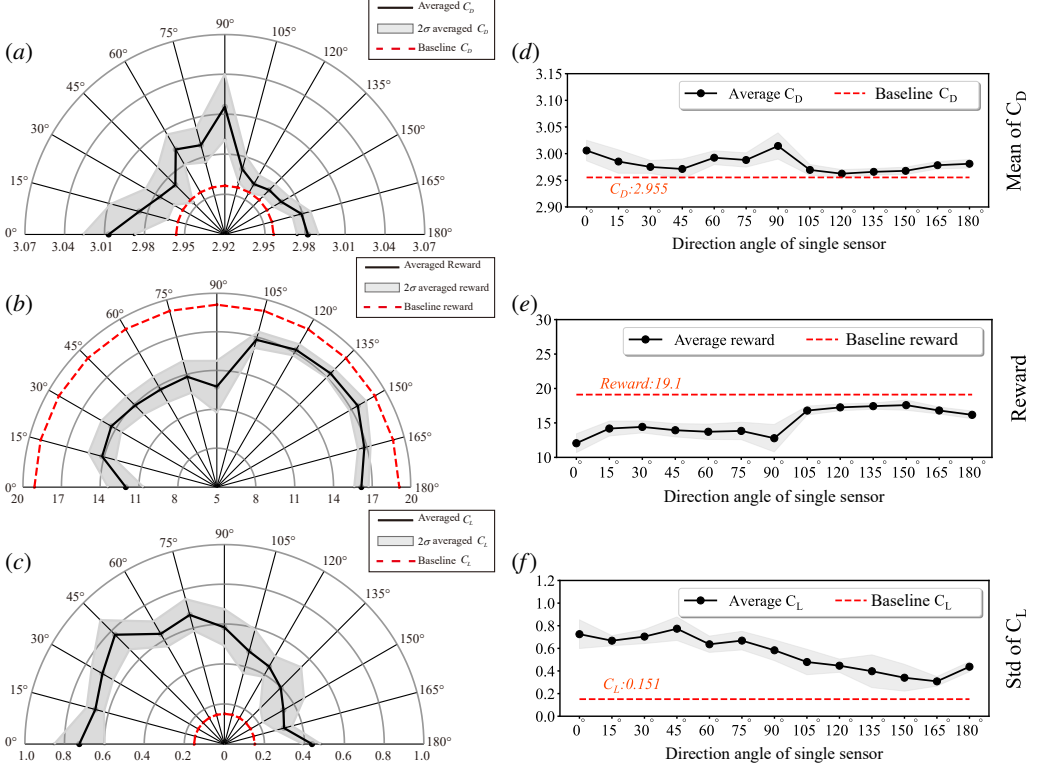


Figure 7: One pressure sensor is placed every 15° on the cylinder surface for training, from 0° to 180° , for a total of 13 sets of training. (a), (b) and (c) are mean drag coefficient C_D , reward, and std lift coefficient C_L in the last 10 training epochs respectively, (d) is the changing trends of mean drag coefficient C_D , reward and std lift coefficient C_L .

and lift reduction. To explore the maximum performance potential of DF-DRL and obtain the optimal sensor layout scheme, single sensor schemes \mathcal{L}_{III} are selected in the following study, as illustrated in Fig. 4(c). According to the symmetry of the geometry of the setup and the boundary conditions, this study only consider deploying sensors on the upper semicircle region for training and analysis purposes. The cylinder surface features a single pressure sensor located every 15° , covering a range of 0° to 180° , with a total of 13 configurations. Three repetitions of the training are performed for each case with the same hyperparameters to eliminate randomness. As shown in Fig. 7(a), the mean drag coefficient C_D indicates that AFC performance with only one pressure sensor is almost as optimal as baseline scheme \mathcal{L}_I . The results suggest that scheme \mathcal{L}_{III} on cylinder surfaces using the DF-DRL method can reach the best performance of active flow control.

It can also be observed from Fig. 7(b), that the trailing edge sensor of the cylinder has a higher reward value compared to the leading edge sensor, resulting in a lower mean drag coefficient. Furthermore, a sudden reduction in the drag coefficient can be observed between \mathcal{L}_{III}^{75} and \mathcal{L}_{III}^{90} . This can be attributed to the influence of jet actuators situated on top side of the cylinder, where changes in jet velocity can lead to abnormal pressure fluctuations on the surface at 90° that confuse the DRL controller. Additionally, a significant jump in performance occurs between \mathcal{L}_{III}^{90} and \mathcal{L}_{III}^{150} , characterized by a marked decrease in the mean drag coefficient and the lift coefficient. A decreasing trend can be observed in the standard deviation of the lift coefficient from \mathcal{L}_{III}^0 to \mathcal{L}_{III}^{180} , as depicted in Fig. 7(c). This further

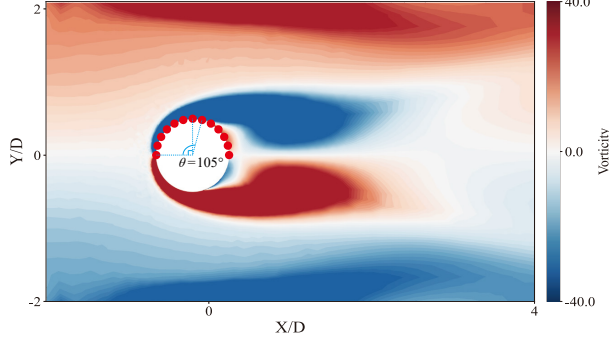


Figure 8: Contours of time-averaged vorticity of a plain case, the red points are surface pressure sensors. Vortex separation occurs between sensors 90° and 105° .

emphasizes that a sensor located closer to the trailing edge of the cylinder can effectively generate information that can be used to mitigate the standard deviation of the lift coefficient.

To provide a more comprehensive explanation of this phenomenon, Fig. 8 depicts the time-averaged vorticity field of the uncontrolled flow around the cylinder, with the red dots representing the 13 different single-sensor layout schemes. The sensors located at the trailing edge of the cylinder, namely \mathcal{L}_{III}^{105} to \mathcal{L}_{III}^{180} , are positioned at the vortex shedding location, indicating that these pressure sensors contain crucial information about vortex shedding compared to the windward side of the cylinder. This observation explains why the trailing edge pressure sensors outperform the leading edge sensors in the overall training outcomes, which include the reduction of drag and lift coefficients.

To summarize, a general tendency of mean drag coefficient, reward, and standard deviation of lift coefficient is presented in Fig. 7(d). Notably, a single sensor situated between 0° and 180° demonstrates near optimal reduced drag and lift coefficients, corresponding to an elevated reward value. These results offer inspiration for the training strategy of a single sensor system \mathcal{L}_{III} at higher Reynolds numbers.

4.3. Robustness of DF-DRL based plant under higher Reynolds number

Based on the promising performance of active flow control demonstrated in §4.2.2, Scheme \mathcal{L}_{III}^{150} is chosen to investigate the robustness of a single surface sensor at higher Reynolds numbers ($Re = 500$ and 1000). The policy network architecture is kept the same as before, consisting of two dense layers of 512 fully connected neurons, with the input layer receiving data from a single pressure sensor, and the output layer representing the jet velocity. As the vortex shedding frequency of the cylinder increases with the rise in Reynolds numbers, the SAC agent interacts with the environment every 44 and 46 time steps at $Re = 500$ and 1000 , respectively.

Figure 9 shows the evolution for the mean drag coefficient, reward value, and lift coefficient obtained from three repeated training processes at Reynolds numbers of $Re = 500$ and 1000 . After approximately 400 episodes at $Re = 500$ and 600 episodes at $Re = 1000$, the drag coefficient approached convergence, demonstrating that a stable control strategy was achieved. Meanwhile, the reward curves gradually increased with each episode with the standard deviation of the lift coefficient declined and then stabilized. As described in Equation 2.4, lift and drag coefficient are both first-order terms, where lift has a weight of 1 and drag has a weight of 0.1. For the deep reinforcement learning agent, this implies that the reduction of drag has a higher reward, and when it is reduced to its maximum value (2.1 at $Re = 500$ and 1.9 at $Re = 1000$, respectively), inhibiting lift becomes the only viable

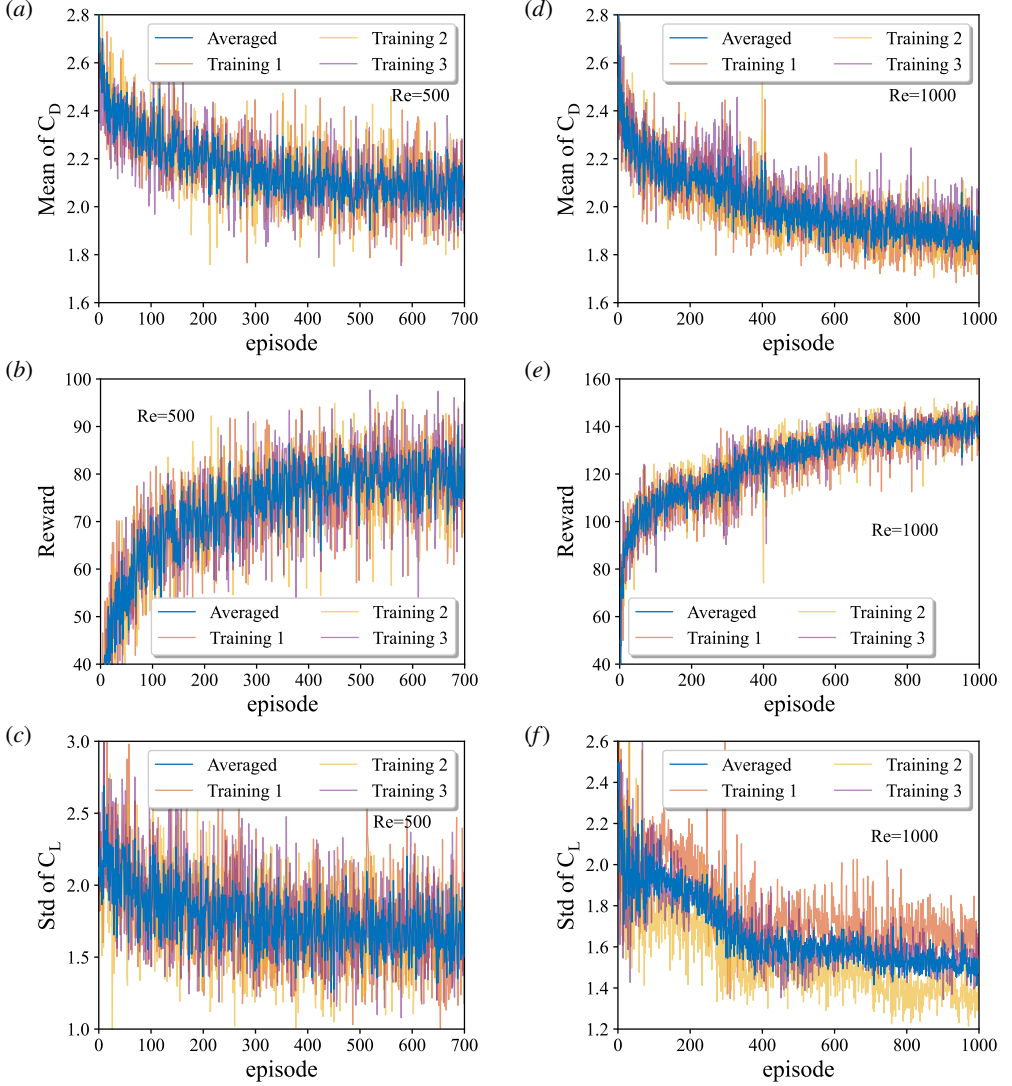


Figure 9: Evolution of mean drag coefficient C_D and reward curves in the learning process at $Re = 500$ [corresponding to (a) and (b)], $Re = 1000$ [corresponding to (c) and (d)]. The averaged curves labeled in blue refer to the moving average of the mean of all three training curves in each subgraph. All results are obtained under scheme \mathcal{L}_{III}^{150} .

option. However, as the Reynolds number increases, the learning requires more episodes to converge, and the agents need more trial-and-error steps to comprehend the nonlinear relationships inherent in the dynamic system.

An interesting phenomenon is observed when comparing the final performance of drag reduction across different Reynolds numbers. As the Reynolds number increases, the drag reduction effect improves. This contradicts our intuition, as we would normally expect the flow field to become more complex at high Reynolds numbers, with increased turbulence and vortex shedding, making it difficult for the DRL agent to learn an effective strategy for flow control. However, this is not the case. The main reason for this lies in the drag force component (Achenbach 1968). The overall drag F_d on the circular cylinder submerged in a

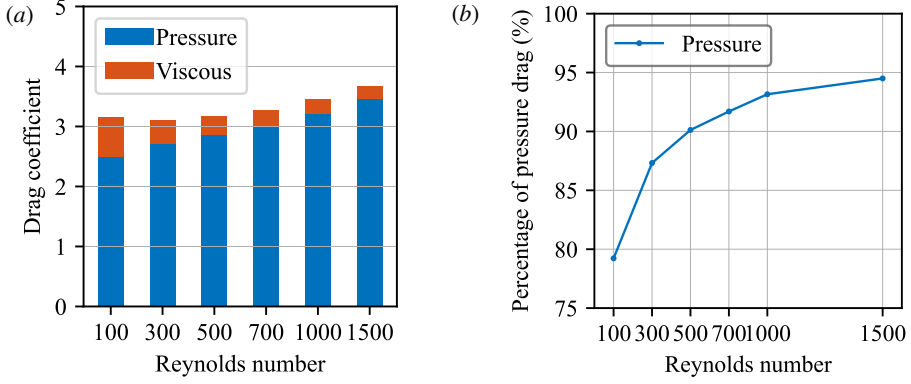


Figure 10: Component analysis of (a) Drag force caused by pressure and skin friction respectively at different Reynolds numbers, and (b) the proportion of pressure drag in the total drag.

Newtonian fluid can be calculated by

$$F_d = \underbrace{\oint p \cdot \cos(\theta) \cdot dA}_{\text{Pressure drag}} + \underbrace{\oint \tau_w \cdot \sin(\theta) \cdot dA}_{\text{Skin friction drag}}, \quad (4.1)$$

$$\tau_w = \mu \cdot \left(\frac{\partial v_t}{\partial n} \right)_{\text{Surface}}, \quad (4.2)$$

where p and τ_w is the normal stress and shear stress act on the cylinder surface, respectively. v_t is the velocity along the cylinder surface, n is normal direction.

Figure 10 shows the magnitudes of pressure drag and skin friction drag, as well as the proportion of pressure drag in total drag, at different Reynolds numbers. It can be observed that, as the Reynolds number increases, the proportion of pressure drag monotonically increases, growing from 79.2% at $Re = 100$ to 94.5% at $Re = 1500$. Under a invariant aerodynamic shape and inflow velocity, the main mechanism of active flow control was to suppress the shedding of vortices at the rear end of the cylinder (Wang & Feng 2018). This indicates that the significant drag reduction effect was mainly attributed to the reduction of pressure drag caused by flow separation. As the Reynolds number increased, the proportion of pressure drag in the overall drag force increased, leading to a more pronounced drag reduction effect if the flow separation is effectively manipulated by the DRL controller.

Tang *et al.* (2020) also proposed a compelling explanation. The flow around a cylinder can be decomposed into a superposition of steady baseflow and vortex shedding components. The baseflow numerically simulated using a symmetric boundary condition at the equatorial plane of the cylinder. The results showed that the drag force on the cylinder controlled by DRL was consistent with the drag force of the baseflow, which indicates that the drag reduction of active flow control using DRL mainly originates from vortex shedding, and the drag generated by vortex shedding is mainly attributable to the pressure drag component. Straightforwardly, under high Reynolds number conditions, the increased drag caused by the pressure component (both in absolute value and proportion) allows the DRL agent to have greater potential for flow control. When the DRL agent finds the optimal control rate, it leads to a decrease in the drag coefficient.

The results of dynamic feature-based soft actor-critic (SAC) algorithm are presented in

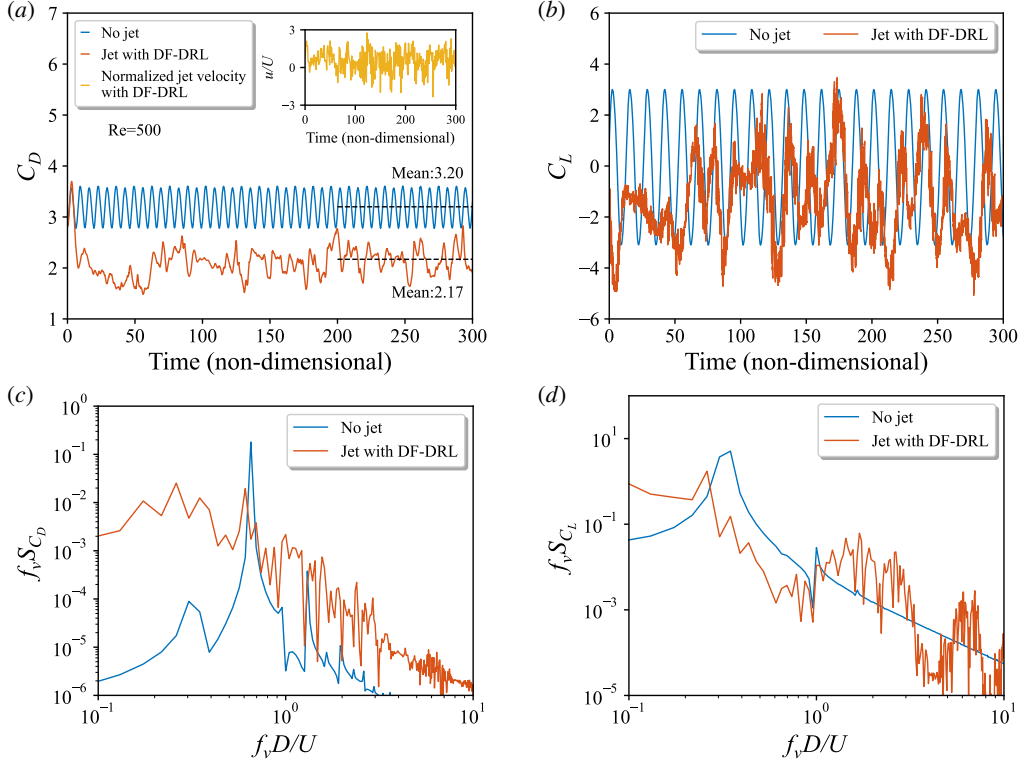


Figure 11: (a) Evolution of drag coefficient C_D for the cylinder without (no jet) and with (DF-DRL cylinder) active flow control at $Re = 500$, as well as the associated normalized velocity flow rate of the jet flow Γ_1 ; (b) Temporal variations in smoothed lift coefficient C_L for the cylinder without (no jet) and with (DRL cylinder) active flow control in $Re = 500$; (c) power spectral density of the drag coefficient C_D during the period of non-dimensional time ranging from 200 to 300; (d) power spectral density of the lift coefficient C_L during the period of non-dimensional time ranging from 200 to 300.

Fig. 11. The entire training process is parallelized across five environments provided by DRLinFluids. The algorithm successfully learned to perform active flow control, resulting in a continuous reduction of drag and suppression of lift. In the absence of actuation, the drag coefficient C_D oscillates periodically around a mean value, as shown in Fig. 11(a). The mean value of C_D is 3.20, with a standard deviation of 0.283 for the drag coefficient and 2.17 for the lift coefficient. With DF-DRL based active flow control, the mean drag coefficient is reduced to 2.17, corresponding to a drag reduction of approximately 32.2%. Furthermore, the fluctuation of the drag coefficient is suppressed, as indicated by the reduced standard deviation value of 0.252. Meanwhile, the standard deviation value of the lift coefficient is slightly reduced to 1.61.

Power spectrum analyses are conducted to compare the drag C_D and lift C_L coefficients of the cylinder with and without active flow control, and the results are presented in Fig. 11(c) and (d). The power spectrum curves for both C_D and C_L of the plain cylinder exhibit a distinct peak. This indicates that there is a series of distinct vortex shedding at this frequency, which contribute to the majority of energy required for the mean drag and the fluctuation. By contrast, the peaks disappear in the power spectrum curves of C_D and C_L of the cylinder with DF-DRL based active flow control.

The results presented in Fig. 12 demonstrate that at a Reynolds number of 1000, the

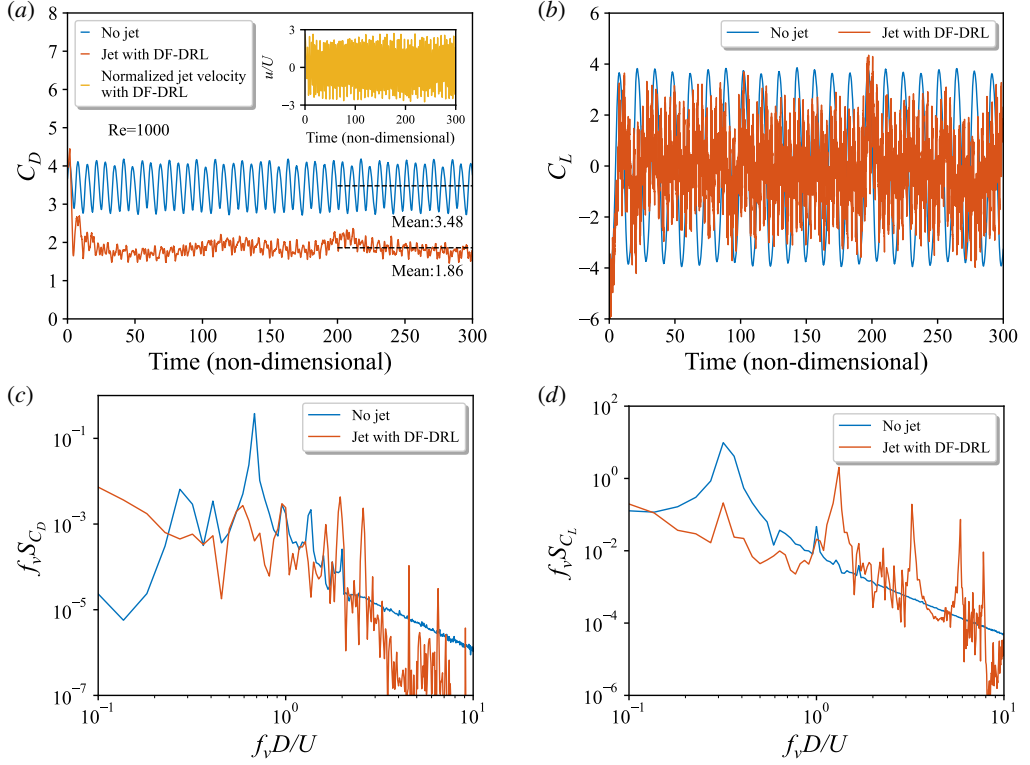


Figure 12: (a) Evolution of drag coefficient C_D for the cylinder without (no jet) and with (DF-DRL cylinder) active flow control at $Re = 1000$, as well as the associated normalized velocity flow rate of the jet flow Γ_1 ; (b) Temporal variations in smoothed lift coefficient C_L for the cylinder without (no jet) and with (DF-DRL cylinder) active flow control at $Re = 1000$; (c) and (d) are power spectral density of the drag coefficient C_D and lift coefficient C_L respectively during the period of non-dimensional time ranging from 200 to 300.

turbulent conditions are relatively weak. Specifically, for the plain cylinder, the mean drag coefficient is measured to be 3.48 with a standard deviation of 0.455. In addition, the lift coefficient exhibits a standard deviation of 2.76. However, when active flow control is implemented, a significant reduction in the mean drag coefficient is achieved, resulting in a value of 1.86, which corresponds to a drag reduction of approximately 46.55%. Moreover, the standard deviation of the drag coefficient decreases to 0.31, indicating a more consistent behavior of the cylinder under flow control. Notably, the standard deviation of the lift coefficient is also markedly reduced to 1.61, which is highly desirable for suppressing the lift force and mitigating flow-induced instability of the cylinder.

The power spectrum analyses of C_D and C_L for the cylinder with and without active flow control are presented in Fig. 12(c) and (d). The power spectrum curves for both C_D and C_L of the plain cylinder shows an obvious peak, indicating the presence of a regular vortex shedding with significant energy. In contrast, when active flow control is implemented, the peak in the power spectrum curves of C_D and C_L for the cylinder is eliminated, indicating that the regular vortex shedding has been completely disrupted by the jet actuation.

Figure 13 displays the instantaneous flow field around a circular cylinder, with and without active control. The impact of controlled jet flow on reducing the aerodynamic force acting on the cylinder is explained in terms of the flow pattern. In Fig. 13(a) and (c), which represent

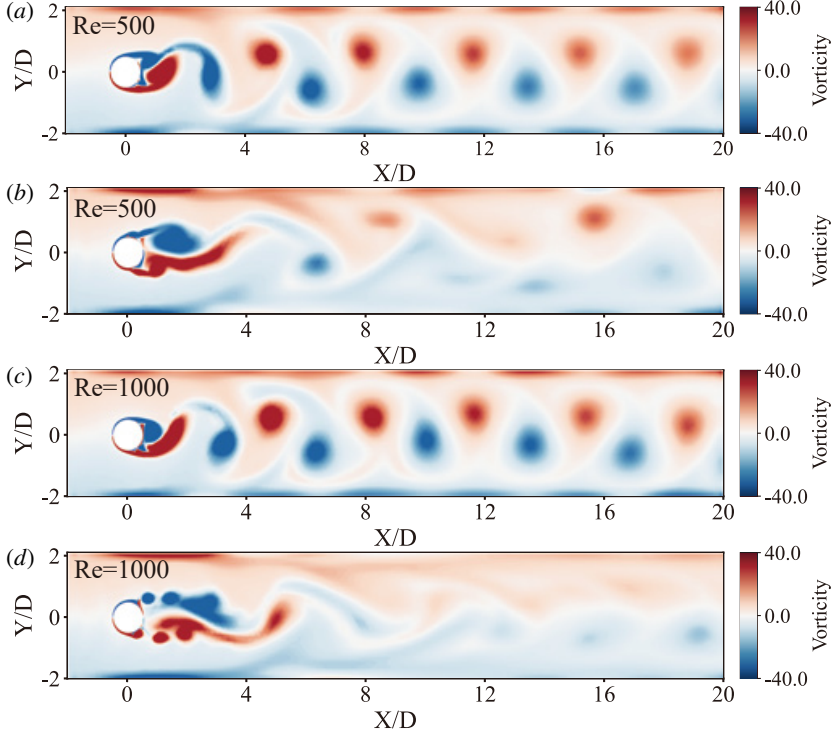


Figure 13: Typical snapshots of the vorticity channel around the cylinder at $Re = 500$ corresponding to the flow without (a) and with (b) control and $Re = 1000$ corresponding to the flow without (c) and with (d) control.

conditions for $Re = 500$ and 1000 , respectively, a vortex shedding pattern is observed for the plain cylinder, as expected. This alternate vortex shedding pattern directly contributes to fluctuations in both the drag and lift coefficients, as demonstrated in Fig. 11 and 12.

Figure 13(b) and (d) illustrate the impact of fluctuating actuation on the vortex shedding pattern. The alternate vortex shedding is suppressed, resulting in reduced fluctuations of both C_D and C_L . Meanwhile, an elongated recirculation bubble is formed in the near wake, which is associated with increased pressure and a reduction in drag force. The elongated wake implies a reduced curvature of the shear layer, which corresponds to increased pressure at the rearward cylinder side. As a result, the cylinder with active flow control experiences less drag.

Figure 14 depicts the mean vorticity contours around a cylinder, with and without active control. The increase in the recirculation zone is very visible at $Re = 500$ and 1000 and illustrates the effective control strategy learned by the DRL agent. The results demonstrate that well-trained DRL agents, which utilize a single surface pressure sensor's temporal information as the state, can achieve efficient control even under flow conditions with strong nonlinearity and various Reynolds numbers.

It is worth noting that learning a DRL-based control law for AFC task presents a significant challenge in utilizing a single surface pressure sensor as the state in weak turbulent conditions. However, these results demonstrate the efficacy of DF-DRL based active flow control of a circular cylinder with sparse surface pressure sensing, and offer a promising avenue for reducing drag and enhancing AFC performance in fluid dynamics systems.

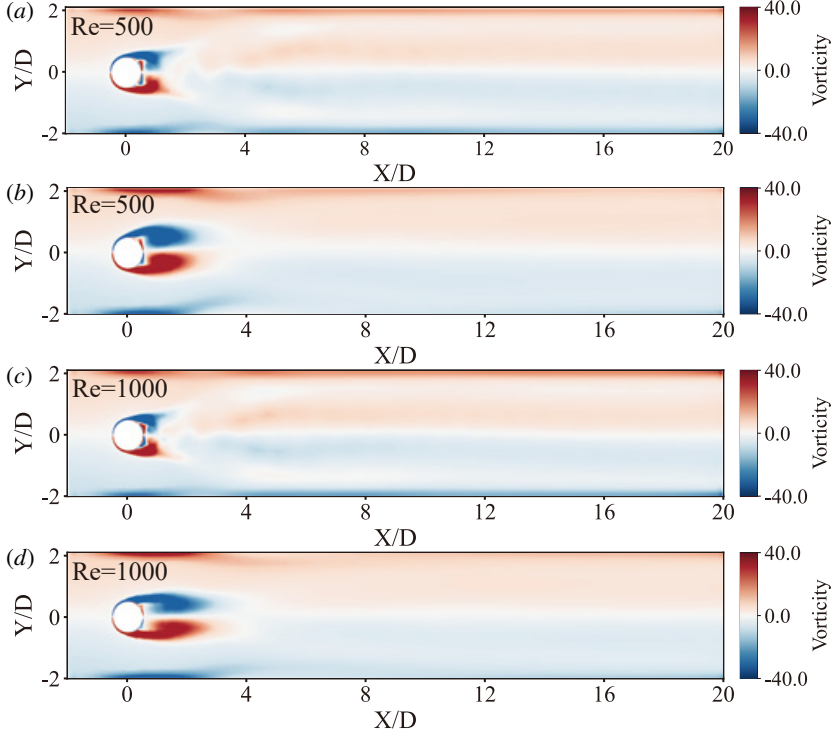


Figure 14: Mean vorticity contours around the cylinder at $Re = 500$ corresponding to the flow without (a) and with (b) control and $Re = 1000$ corresponding to the flow without (c) and with (d) control.

5. Conclusions and outlook

This study presents significant progress towards practical active flow control with surface pressure sensor located on a circular cylinder as sole input for a DRL agent. This approach has potential for advancements in deep reinforcement learning for real-world applications, such as drag and lift reduction for vehicle and high-rise building. The main results of this study are summarized as follows.

Firstly, a novel deep reinforcement learning method called Dynamic Feature-Based Deep Reinforcement Learning (DF-DRL) is introduced. Essentially, DF-DRL utilizes prior knowledge to extract one or several features of a nonlinear dynamic system, enabling it to estimate the complete state of the system to the fullest extent possible. This concept aligns with the ideas of pattern recognition and reduced order modelling. The DF-DRL model combines identification and control, which is not limited to the traditional DRL tasks that take the state at a certain moment as input. Instead, suitable dynamic feature states are selected and lifted to a higher dimensional vector based on the characteristics of different dynamic systems. Following this step, the vector is used as the state input to the agent. Results show that using DF-DRL with a single surface pressure sensor can achieve the same drag reduction performance as vanilla DRL method using 147 velocity sensors that fully sample the cylinder wake region.

Secondly, the study investigates the distribution of sensors needed for active flow control of cylinder wake. We conclude that in low to moderate Reynolds number scenarios, a single surface pressure sensor can achieve control results comparable to those obtained with 147 wake sensors under active flow control when DF-DRL is used. Additionally, we find that the

reward value obtained with a single trailing edge sensor on the cylinder is higher than if the sensor is located at the leading edge, resulting in a lower mean drag coefficient and standard deviation of the lift coefficient.

Thirdly, two different flow situations were examined to verify the effectiveness and robustness of the proposed sensor configuration and DF-DRL method. Results show that the deep reinforcement learning agent utilizing a single surface pressure sensor is capable of controlling wake development behind the circular cylinder, even under more complex scenarios corresponding to higher Reynolds numbers.

Sparse reduced-order modeling (Brunton *et al.* 2016b; Loiseau *et al.* 2018a) is a highly popular research field, in which selecting appropriate dynamic feature lifting methods for different fluid dynamic systems can enable more accurate estimation using fewer sensor data. Processing these features and using them as DRL states is a promising approach. In the present study, significant reductions in the drag coefficient of a cylinder are achieved through two distinct approaches. Specifically, the use of typical DRL resulted in a reduction of 6.4% utilizing a 4 sensor layout scheme, while dynamic feature sensing with lifting, yielded an even greater reduction of 8.0% comparing against the benchmark performance. Importantly, the results of this investigation demonstrate that the drag coefficient of the dynamic feature sensing with lifting and DRL (DF-DRL) model is impressively lower than the vanilla model that relies solely on direct sensor feedback. In particular, the DF-DRL model exhibited a reduction of 25% in the drag coefficient, highlighting the efficacy of this approach for improving aerodynamic performance. The DF-DRL method presents a promising approach to significantly reducing the number of required sensors while achieving optimal drag and lift coefficient reduction performance, which offers a promising pathway for taming complex fluid dynamics systems.

Acknowledgement

This study is supported by the National Key R&D Program of China (2021YFC3100702), National Natural Science Foundation of China (52278493, 52108451), Shenzhen Science and Technology Program (SGDX20210823103202018, GXWD20201230155427003-20200823230021001, KQTD20210811090112003), and Guangdong-Hong Kong-Macao Joint Laboratory for Data-Driven Fluid Mechanics and Engineering Applications (2020B1212030001). This work is also supported by the National Science Foundation of China (NSFC) through grants 12172109 and 12172111, by Guangdong province, China, via the Natural Science and Engineering grant 2022A1515011492 and by the Shenzhen Research Foundation for Basic Research, China, through grant JCYJ20220531095605012.

REFERENCES

- ACHENBACH, E. 1968 Distribution of local pressure and skin friction around a circular cylinder in cross-flow up to $Re = 5 \times 10^6$. *Journal of Fluid Mechanics* **34** (4), 625–639.
- ANDRYCHOWICZ, MARCIN, WOLSKI, FILIP, RAY, ALEX, SCHNEIDER, JONAS, FONG, RACHEL, WELINDER, PETER, MCGREW, BOB, TOBIN, JOSH, ABBEEL, PIETER & ZAREMBA, WOJCIECH 2018 Hindsight Experience Replay, arXiv: 1707.01495.
- BELLEMARE, MARC G., DABNEY, WILL & MUNOS, RÉMI 2017 A Distributional Perspective on Reinforcement Learning, arXiv: 1707.06887.
- BOURGEOIS, J. A., MARTINUZZI, R. J. & NOACK, B. R. 2013 Generalised phase average with applications to sensor-based flow estimation of the wall-mounted square cylinder wake. *J. Fluid Mech.* **736**, 316–350.
- BRUNTON, STEVEN L., BRUNTON, BINGNI W., PROCTOR, JOSHUA L., KAISER, EURIKA & KUTZ, J. NATHAN 2017 Chaos as an intermittently forced linear system. *Nature Communications* **8** (1), 19.

- BRUNTON, STEVEN L., BRUNTON, BINGNI W., PROCTOR, JOSHUA L. & KUTZ, J. NATHAN 2016a Koopman Invariant Subspaces and Finite Linear Representations of Nonlinear Dynamical Systems for Control. *PLOS ONE* **11** (2), e0150171.
- BRUNTON, S. L. & NOACK, B. R. 2015 Closed-loop turbulence control: Progress and challenges. *Appl. Mech. Rev.* **67** (5), 050801:01–48.
- BRUNTON, S. L., PROCTOR, J. L. & KUTZ, N. J. 2016b Discovering governing equations from data by sparse identification of nonlinear dynamical systems. *Proc. Natl. Acad. Sci. USA* **113** (5), 3932–3937.
- DURIEZ, THOMAS, BRUNTON, STEVEN L. & NOACK, BERND R. 2017 *Machine learning control-taming nonlinear dynamics and turbulence*, , vol. 116. Springer.
- FAN, DIXIA, YANG, LIU, WANG, ZHICHENG, TRIANTAFYLLOU, MICHAEL S. & KARNIADAKIS, GEORGE EM 2020 Reinforcement learning for bluff body active flow control in experiments and simulations. *Proceedings of the National Academy of Sciences* **117** (42), 26091–26098.
- FRANÇOIS-LAVET, VINCENT, HENDERSON, PETER, ISLAM, RIASHAT, BELLEMARE, MARC G. & PINEAU, JOELLE 2018 An introduction to deep reinforcement learning. *arXiv preprint arXiv:1811.12560* , arXiv: 1811.12560.
- FUJIMOTO, SCOTT, VAN HOOF, HERKE & MEGER, DAVID 2018 Addressing Function Approximation Error in Actor-Critic Methods. *arXiv:1802.09477 [cs, stat]* , arXiv: 1802.09477.
- GARNIER, PAUL, VIQUERAT, JONATHAN, RABAULT, JEAN, LARCHER, AURÉLIEN, KUHNLE, ALEXANDER & HACHEM, ELIE 2021 A review on deep reinforcement learning for fluid mechanics. *Computers & Fluids* **225**, 104973.
- GAUTIER, NICOLAS, AIDER, J-L, DURIEZ, THOMAS, NOACK, BEND R, SEGOND, MARC & ABEL, MARKUS 2015 Closed-loop separation control using machine learning. *Journal of Fluid Mechanics* **770**, 442–457.
- GUASTONI, LUCA, RABAULT, JEAN, SCHLATTER, PHILIPP, AZIZPOUR, HOSSEIN & VINUESA, RICARDO 2023 Deep reinforcement learning for turbulent drag reduction in channel flows. *Eur. J. Phys., To Appear. Preprint arXiv:2301.09889* .
- HA, DAVID & SCHMIDHUBER, JÜRGEN 2018 World Models. *arXiv:1803.10122 [cs, stat]* , arXiv: 1803.10122.
- HAARNOJA, TUOMAS, ZHOU, AURICK, ABBEEL, PIETER & LEVINE, SERGEY 2018 Soft actor-critic: Off-policy maximum entropy deep reinforcement learning with a stochastic actor. In *International conference on machine learning*, pp. 1861–1870. PMLR.
- HERVÉ, A., SIPP, D., SCHMID, P. J. & SAMUELIDES, M. 2012 A physics-based approach to flow control using system identification. *J. Fluid Mech.* **702**, 26–58.
- JASAK, HRVOJE, JEMCOV, ALEKSANDAR & TUKOVIC, ZELJKO 2007 Openfoam: A c++ library for complex physics simulations. In *International workshop on coupled methods in numerical dynamics*, , vol. 1000, p. 1–20. IUC Dubrovnik Croatia.
- KIRAN, B RAVI, SOBH, IBRAHIM, TALPAERT, VICTOR, MANNION, PATRICK, SALLAB, AHMAD A. AL, YOGAMANI, SENTHIL & PÉREZ, PATRICK 2022 Deep Reinforcement Learning for Autonomous Driving: A Survey. *IEEE Transactions on Intelligent Transportation Systems* **23** (6), 4909–4926.
- KORKISCHKO, IVAN & MENEGHINI, JULIO ROMANO 2012 Suppression of vortex-induced vibration using moving surface boundary-layer control. *Journal of Fluids and Structures* **34**, 259–270.
- KUHNLE, ALEXANDER, SCHAARSCHMIDT, MICHAEL & FRICKE, KAI 2017 Tensorforce: a tensorflow library for applied reinforcement learning. Web page.
- LEE, CHANGHOON, KIM, JOHN, BABCOCK, DAVID & GOODMAN, RODNEY 1997 Application of neural networks to turbulence control for drag reduction. *Physics of Fluids* **9** (6), 1740–1747, publisher: American Institute of Physics.
- LI, SHAOPENG, SNAIKI, REDA & WU, TENG 2021 A knowledge-enhanced deep reinforcement learning-based shape optimizer for aerodynamic mitigation of wind-sensitive structures. *Computer-Aided Civil and Infrastructure Engineering* **36** (6), 733–746.
- LILLICRAP, TIMOTHY P., HUNT, JONATHAN J., PRITZEL, ALEXANDER, HEESS, NICOLAS, EREZ, TOM, TASSA, YUVAL, SILVER, DAVID & WIERSTRA, DAAN 2019 Continuous control with deep reinforcement learning. *arXiv:1509.02971 [cs, stat]* , arXiv: 1509.02971.
- LOISEAU, J.-CH., NOACK, B. R. & BRUNTON, S. L. 2018a Sparse reduced-order modeling: Sensor-based dynamics to full-state estimation. *J. Fluid Mech.* **844**, 459–490.
- LOISEAU, JEAN-CHRISTOPHE, NOACK, BERND R. & BRUNTON, STEVEN L. 2018b Sparse reduced-order modelling: Sensor-based dynamics to full-state estimation. *Journal of Fluid Mechanics* **844**, 459–490.
- MEI, YU-FEI, ZHENG, CHUN, AUBRY, NADINE, LI, MENG-GE, WU, WEI-TAO & LIU, XIANGLEI 2021 Active

- control for enhancing vortex induced vibration of a circular cylinder based on deep reinforcement learning. *Physics of Fluids* **33** (10), 103604.
- MEZIĆ, IGOR 2005 Spectral Properties of Dynamical Systems, Model Reduction and Decompositions. *Nonlinear Dynamics* **41** (1), 309–325.
- MNIH, VOLODYMYR, BADIA, ADRIA PUIGDOMENECH, MIRZA, MEHDI, GRAVES, ALEX, LILICRAP, TIMOTHY, HARLEY, TIM, SILVER, DAVID & KAVUKCUOGLU, KORAY 2016 Asynchronous Methods for Deep Reinforcement Learning. In *International Conference on Machine Learning*, pp. 1928–1937. PMLR.
- MNIH, VOLODYMYR, KAVUKCUOGLU, KORAY, SILVER, DAVID, GRAVES, ALEX, ANTONOGLU, IOANNIS, WIERSTRA, DAAN & RIEDMILLER, MARTIN 2013 Playing Atari with Deep Reinforcement Learning. *arXiv:1312.5602 [cs]*, arXiv: 1312.5602.
- NGUYEN, HAI & LA, HUNG 2019 Review of Deep Reinforcement Learning for Robot Manipulation. In *2019 Third IEEE International Conference on Robotic Computing (IRC)*, pp. 590–595.
- NOVATI, GUIDO, VERMA, SIDDHARTHA, ALEXEEV, DMITRY, ROSSINELLI, DIEGO, REES, VAN WIM M. & KOUMOUTSAKOS, PETROS 2017 Synchronisation through learning for two self-propelled swimmers. *Bioinspiration & Biomimetics* **12** (3), 036001.
- PARIS, ROMAIN, BENEDDINE, SAMIR & DANDOIS, JULIEN 2021 Robust flow control and optimal sensor placement using deep reinforcement learning. *Journal of Fluid Mechanics* **913**.
- PINO, FABIO, SCHENA, LORENZO, RABAULT, JEAN & MENDEZ, MIGUEL A 2023 Comparative analysis of machine learning methods for active flow control. *Journal of Fluid Mechanics* **958**, A39.
- QIN, SHENG, WANG, SHUYUE, RABAULT, JEAN & SUN, GANG 2021 An application of data driven reward of deep reinforcement learning by dynamic mode decomposition in active flow control. *arXiv preprint arXiv:2106.06176*.
- RABAULT, JEAN, KUCHTA, MIROSLAV, JENSEN, ATLE, RÉGLADE, ULYSSE & CERARDI, NICOLAS 2019 Artificial neural networks trained through deep reinforcement learning discover control strategies for active flow control. *Journal of Fluid Mechanics* **865**, 281–302.
- RABAULT, JEAN & KUHNLE, ALEXANDER 2019 Accelerating deep reinforcement learning strategies of flow control through a multi-environment approach. *Physics of Fluids* **31** (9), 094105.
- REN, FENG, RABAULT, JEAN & TANG, HUI 2021a Applying deep reinforcement learning to active flow control in weakly turbulent conditions. *Physics of Fluids* **33** (3), 037121.
- REN, FENG, WANG, CHENGLEI & TANG, HUI 2019 Active control of vortex-induced vibration of a circular cylinder using machine learning. *Physics of Fluids* **31** (9), 093601.
- REN, FENG, WANG, CHENGLEI & TANG, HUI 2021b Bluff body uses deep-reinforcement-learning trained active flow control to achieve hydrodynamic stealth. *Physics of Fluids* **33** (9), 093602.
- SCHÄFER, MICHAEL, TÜRK, STEFAN, DURST, FRANZ, KRAUSE, EGON & RANNACHER, ROLF 1996 Benchmark computations of laminar flow around a cylinder. In *Flow simulation with high-performance computers II*, pp. 547–566. Springer.
- SCHULMAN, JOHN, LEVINE, SERGEY, MORITZ, PHILIPP, JORDAN, MICHAEL I. & ABBEEL, PIETER 2017a Trust Region Policy Optimization, arXiv: 1502.05477.
- SCHULMAN, JOHN, WOLSKI, FILIP, DHARIWAL, PRAFULLA, RADFORD, ALEC & KLIMOV, OLEG 2017b Proximal policy optimization algorithms. *arXiv:1707.06347 [cs]*.
- SILVER, DAVID, HUBERT, THOMAS, SCHRITTWIESER, JULIAN, ANTONOGLU, IOANNIS, LAI, MATTHEW, GUEZ, ARTHUR, LANCTOT, MARC, SIFRE, LAURENT, KUMARAN, DHARSHAN, GRAEPEL, THORE, LILICRAP, TIMOTHY, SIMONYAN, KAREN & HASSABIS, DEMIS 2017 Mastering Chess and Shogi by Self-Play with a General Reinforcement Learning Algorithm. *arXiv:1712.01815 [cs]*, arXiv: 1712.01815.
- TAKENS, FLORIS 1981 Detecting strange attractors in turbulence. In *Dynamical Systems and Turbulence, Warwick 1980* (ed. David Rand & Lai-Sang Young), *Lecture Notes in Mathematics*, pp. 366–381. Berlin, Heidelberg: Springer.
- TANG, HONGWEI, RABAULT, JEAN, KUHNLE, ALEXANDER, WANG, YAN & WANG, TONGGUANG 2020 Robust active flow control over a range of reynolds numbers using an artificial neural network trained through deep reinforcement learning. *Physics of Fluids* **32** (5), 053605.
- VARELA, PAU, SUÁREZ, POL, ALCÁNTARA-ÁVILA, FRANCISCO, MIRÓ, ARNAU, RABAULT, JEAN, FONT, BERNAT, GARCÍA-CUEVAS, LUIS MIGUEL, LEHMKUHL, ORIO & VINUESA, RICARDO 2022 Deep reinforcement learning for flow control exploits different physics for increasing reynolds number regimes. In *Actuators*, , vol. 11, p. 359. Multidisciplinary Digital Publishing Institute.
- VERMA, SIDDHARTHA, NOVATI, GUIDO & KOUMOUTSAKOS, PETROS 2018 Efficient collective swimming by harnessing vortices through deep reinforcement learning. *Proceedings of the National Academy of Sciences* **115** (23), 5849–5854.

- VIGNON, COLIN, RABAULT, JEAN & VINUESA, RICARDO 2023 Recent advances in applying deep reinforcement learning for flow control: Perspectives and future directions. *Physics of Fluids* **35** (3), 031301.
- VIQUERAT, JONATHAN, RABAULT, JEAN, KUHNLE, ALEXANDER, GHRAIEB, HASSAN, LARCHER, AURÉLIEN & HACHEM, ELIE 2021 Direct shape optimization through deep reinforcement learning. *Journal of Computational Physics* **428**, 110080.
- WANG, JINJUN & FENG, LIHAO 2018 *Flow Control Techniques and Applications*. Cambridge Aerospace Series . Cambridge: Cambridge University Press.
- WANG, QIULEI, YAN, LEI, HU, GANG, LI, CHAO, XIAO, YIQING, XIONG, HAO, RABAULT, JEAN & NOACK, BERND R 2022 Drlinfluids: An open-source python platform of coupling deep reinforcement learning and openfoam. *Physics of Fluids* **34** (8), 081801.
- WEBER, THÉOPHANE, RACANIÈRE, SÉBASTIEN, REICHERT, DAVID P., BUESING, LARS, GUEZ, ARTHUR, REZENDE, DANILO JIMENEZ, BADIA, ADRIA PUIGDOMÈNECH, VINYALS, ORIOL, HEES, NICOLAS, LI, YUJIA, PASCANU, RAZVAN, BATTAGLIA, PETER, HASSABIS, DEMIS, SILVER, DAVID & WIERSTRA, DAAN 2018 Imagination-Augmented Agents for Deep Reinforcement Learning. *arXiv:1707.06203 [cs, stat]*, arXiv: 1707.06203.
- WENG, JIAYI, CHEN, HUAYU, YAN, DONG, YOU, KAICHAO, DUBURCQ, ALEXIS, ZHANG, MINGHAO, SU, YI, SU, HANG & ZHU, JUN 2022 Tianshou: A highly modularized deep reinforcement learning library. *Journal of Machine Learning Research* **23** (267), 1–6.
- XU, HUI, ZHANG, WEI, DENG, JIAN & RABAULT, JEAN 2020 Active flow control with rotating cylinders by an artificial neural network trained by deep reinforcement learning. *Journal of Hydrodynamics* **32**, 254–258.
- ZHENG, CHANGDONG, JI, TINGWEI, XIE, FANGFANG, ZHANG, XINSHUAI, ZHENG, HONGYU & ZHENG, YAO 2021 From active learning to deep reinforcement learning: Intelligent active flow control in suppressing vortex-induced vibration. *Physics of Fluids* **33** (6), 063607.
- ZHOU, YU, FAN, DEWEI, ZHANG, BINGFU, LI, RUIYING & NOACK, BERND R 2020 Artificial intelligence control of a turbulent jet. *Journal of Fluid Mechanics* **897**, A27.